

Ultrastable Optical Magnetometry

Nathanial Wilson,* Philip Light, André Luiten, and Christopher Perrella

Institute for Photonics and Advanced Sensing (IPAS), and School of Physical Sciences, The University of Adelaide, South Australia 5005, Australia



(Received 19 November 2018; revised manuscript received 21 January 2019; published 11 April 2019)

We report on an ultrastable optical magnetometer based on nonlinear magneto-optical rotation in ^{87}Rb vapor. The atomic vapor is both optically pumped and probed on the $F = 2 \rightarrow F' = 1$ hyperfine transition of the D_1 manifold. A measurement over 26 h quantifies the magnetometer's performance across 8 orders of magnitude in the Fourier-frequency domain, allowing us to measure the magnetic response into the microhertz domain. We demonstrate a room-temperature sensitivity floor of $15 \text{ fT}_{\text{rms}}/\sqrt{\text{Hz}}$ at a magnetic-field strength of $2.5 \mu\text{T}$, which corresponds to a record $9 \text{ ppb}/\sqrt{\text{Hz}}$ fractional sensitivity. The magnetometer's performance is photon shot-noise limited from 40 Hz to 10 kHz, while below 40 Hz it slowly degrades as approximately $f^{-1/4}$. At 1 mHz the performance is still better than $1 \text{ pT}_{\text{rms}}/\sqrt{\text{Hz}}$. We show that this worsening performance is not a characteristic of the sensor, but instead associated with minute fluctuations of the magnetic field at the sensor from various identified sources.

DOI: [10.1103/PhysRevApplied.11.044034](https://doi.org/10.1103/PhysRevApplied.11.044034)

I. INTRODUCTION

Optical magnetometers are presently among the most sensitive devices for measuring magnetic fields; their sensitivities can rival [1] or even surpass [2–4] that of superconducting quantum interference devices (SQUIDs). With their intrinsic accuracy, room-temperature operability, and portability, these devices are finding applications in numerous fields ranging from medical diagnostics and imaging [5–15], to geomagnetism [4], and fundamental physics research [16–19].

Optical magnetometers come in a number of flavors, each with characteristic advantages and disadvantages. Perhaps the two most frequently encountered flavors make use of the nonlinear magneto-optical rotation (NMOR) [20] or spin-exchange relaxation-free (SERF) [21] techniques. SERF magnetometers have demonstrated magnetic sensitivities below $1 \text{ fT}_{\text{rms}}/\sqrt{\text{Hz}}$ [2–4]; however, they can only operate in near-zero magnetic field ($\lesssim 1 \text{ nT}$) and have a relatively low bandwidth. These aspects limit their practicality in many real-world applications. In contrast, NMOR magnetometers, utilizing frequency [22,23], amplitude [1,24], or polarization [25] modulated-pumping techniques, can operate in magnetic fields higher than that of Earth [22,26]. The absolute sensitivity of NMOR magnetometers is generally 1 to 2 orders of magnitude worse than that of their SERF counterparts.

The sensitivity of an optical magnetometer is subject to two fundamental limits [27–29]: spin-projection noise

and photon shot noise. For NMOR magnetometers, photon shot noise always dominates over spin-projection noise, and sets the performance limit of a well-designed magnetometer at relatively high frequencies ($\gtrsim 10 \text{ Hz}$). However, at low frequencies a number of technical-noise sources typically limit the magnetometer's performance, or the ability to measure that performance, such that one cannot achieve this fundamental limit. These technical-noise sources include fluctuations in optical power (both pump and probe), optical-polarization drift, ambient-field fluctuations, electronic noise in the detection, magnetic-shield noise etc. This can prevent the application of a magnetometer in circumstances that demand high performance at low frequencies. Examples would include magnetic anomaly detection [30], earthquake monitoring [31–33], and the search for plant biomagnetism [34].

In this work, we demonstrate an optical magnetometer, which operates at room temperature and exhibits high sensitivity over a broad range of Fourier frequencies. We generate a magnetic field of $2.5 \mu\text{T}$ within a magnetic shield and subsequently measure that field with a shot-noise-limited sensitivity of $15 \text{ fT}_{\text{rms}}/\sqrt{\text{Hz}}$. This corresponds to a record fractional sensitivity of $9 \text{ ppb}/\sqrt{\text{Hz}}$. Over a 26-h measurement, the measured magnetic field drifts by only 100 ppm, and this instability arises in the applied field rather than from the sensor itself. The result presented here is, to the best of our knowledge, the most sensitive magnetic-field measurement performed by an NMOR magnetometer over an exceptionally broad range of Fourier frequencies from $100 \mu\text{Hz}$ to 10 kHz [1,35], as well as the highest dynamic-range measurement performed by an optical magnetometer of any kind. The fractional

*nathanial.wilson@adelaide.edu.au

sensitivity reported here is around 2 orders of magnitude superior to the best reported measurements with a SERF magnetometer [2–4].

When compared to state-of-the-art superconducting quantum-interference devices, the reported performance is only a factor of 40 inferior to the best-ever reported result at high frequencies [36], and less than 2 orders of magnitude worse at ultralow frequencies around $100 \mu\text{Hz}$ [37]. However, the optical approach reported here benefits from avoiding cryogenics and giving an intrinsically accurate measurement. This demonstration of low-frequency performance of an optical magnetometer opens the potential for many new applications, which are currently dominated by the use of SQUIDs.

II. MAGNETOMETER CONCEPT

The magnetometer utilizes amplitude-modulated non-linear magneto-optical rotation (AMOR) [20,24], in which resonant, linearly polarized light produces spin coherence in an alkali vapor through periodic optical pumping. Pumping with linearly polarized light generates atomic alignment (a rank-two polarization moment) [38]. Using an atomic description in which the quantization axis is aligned with the applied magnetic field, this corresponds to a symmetric distribution of population between Zeeman sublevels with respect to the $|m_F = 0\rangle$ state, and coherences between ground-state Zeeman sublevels of $\Delta m_F = 2$ [22].

When exposed to a weak longitudinal magnetic field, the energy levels of the Zeeman states are shifted by the Larmor frequency, $\Omega_L = \mu_B g_F B / \hbar$, where μ_B is the Bohr magneton, g_F is the hyperfine Landé g -factor, B is the magnetic-field strength and \hbar is the reduced Planck constant. This energy splitting induces temporal evolution of the $\Delta m_F = 2$ coherences at a frequency of $2\Omega_L$ [39], yielding a modulation of the complex refractive indices for the two polarization eigenmodes [28] (circular birefringence). This consequently modulates the polarization plane of a linearly polarized probe beam at the same frequency [27,40]. One finds a strong resonant pumping condition, which maximizes the atomic alignment within the vapor, if the pump beam is modulated at a frequency $\Omega_m = 2\Omega_L$. A measurement of the frequency of this resonant condition allows accurate estimation of the local magnetic-field strength.

III. EXPERIMENTAL SETUP

The experimental setup is presented in Fig. 1. Isotopically pure ^{87}Rb is contained in a cylindrical vapor cell with a 40-mm diameter and 40-mm length. The walls of the cell are coated with paraffin in order to preserve coherences between ground-state Zeeman sublevels, with a measured transverse spin-relaxation time of $T_2 = 36.5 \text{ ms}$. The cell remains at room temperature ($23.10 \pm 0.04^\circ\text{C}$), and is

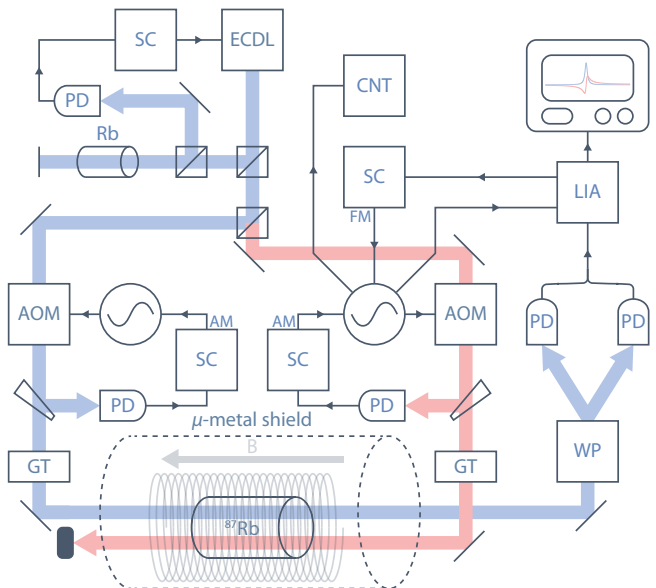


FIG. 1. Simplified experimental setup, showing the external cavity diode laser (ECDL), acousto-optic modulator (AOM), Glan-Thompson prism (GT), Wollaston prism (WP), photodetector (PD), lock-in amplifier (LIA), servo controller (SC), and frequency counter (CNT). The probe beam is shown in blue, while the pump beam is shown in red. All relevant electronic components are referenced to the 10-MHz output of a cesium atomic clock. The AM and FM labels denote amplitude and frequency modulation, respectively.

housed within a six-layer cylindrical μ -metal magnetic shield that has a calculated shielding factor of 2×10^5 [41]. A constant-bias magnetic field of $2.5 \mu\text{T}$ is generated along the longitudinal axis of the cell using a solenoid installed within the innermost shield. This value is chosen as it is the strongest magnetic field that could be applied without deteriorating the magnetometer's performance via gradient broadening [42] due to the inhomogeneity of the field generated by the solenoid.

The solenoid is driven by an ultralow-noise power supply, which produces a fixed voltage with a square-root Allan variance [43] of 3×10^{-8} at 1 s, slowly degrading to 10^{-6} for integration times of 10^4 s. In order to obtain fractional current fluctuations in the part-per-billion range at high Fourier frequencies, the output voltage of the power supply is filtered prior to driving the solenoid using a first-order Butterworth filter with a cut-off frequency of 0.3 mHz. The solenoid current is set by series resistors with an ultralow temperature coefficient of 200 ppb/ $^\circ\text{C}$. The current noise after the filter is below the level that can be measured by any conventional instrumentation and is seen not to limit the magnetometer performance above 10 mHz. Below this frequency, we observe a temperature dependence in the Butterworth filter that causes unwanted current fluctuations that can be observed by the magnetometer.

The atomic vapor is optically pumped and probed on the $5^2S_{1/2} \rightarrow 5^2P_{1/2}$ (D_1) transition of ^{87}Rb by an external cavity diode laser tuned near 795 nm. The laser is frequency locked to the $F = 2 \rightarrow F' = 1$ hyperfine transition using saturated absorption spectroscopy in a reference cell. Both pump and probe beams pass through acousto-optic modulators (AOMs) that downshift their frequencies by 80 MHz, and are also used to control the optical power incident on the vapor cell. The AOM for the pump beam also applies a square-wave amplitude modulation at $\Omega_m/2\pi \approx 34.7$ kHz, with a modulation depth of 100% and a duty cycle of 20%. This amplitude modulation resonantly drives the polarization of the medium.

Prior to the vapor cell, a small fraction of the pump and probe beams is detected by two separate photodetectors. These signals are used to keep the power of each beam stabilized by actively controlling the rf driving power of the AOMs. As the pump beam is amplitude modulated, the photodetector signal is demodulated at $\Omega_m/2\pi$ using a lock-in amplifier referenced to the pump modulation frequency prior to being fed into the power servo. Following stabilization, the square-root Allan variance of the pump and probe powers is relatively flat (i.e., independent of integration time) and below 10^{-4} for integration times ranging between 0.2 and 400 s.

We note that optical-power fluctuations can result in small changes in the observed Larmor frequency through optical saturation and other nonlinear optical effects. Without sufficient power stabilization, this has the effect of giving rise to a fictitious magnetic field. We measure the sensitivity of the magnetometer to these effects by intentionally inducing a large power modulation, and measuring the magnetometer response. Using this sensitivity, we calculate that the stabilized pump and probe beams induce fictitious magnetic fluctuations with a flicker-noise characteristic, the magnitude of which is $1 \text{ fT}_{\text{rms}}/\sqrt{\text{Hz}}$ and $100 \text{ fT}_{\text{rms}}/\sqrt{\text{Hz}}$ at 1 mHz for the pump and probe beams, respectively. These unwanted fluctuations are not a dominant limitation of the magnetometer presented here.

Immediately prior to entering the cell, the pump beam is vertically polarized by a Glan-Thompson (GT) prism and set to propagate parallel to the magnetic field. The probe beam is linearly polarized at 45° from the vertical by a GT prism, and propagates antiparallel to the magnetic field. Both pump and probe beams have a $1/e^2$ diameter of 1.5 mm, and are horizontally displaced by approximately 10 mm relative to each other.

The stability of the polarization of the probe beam is an important quantity, as fluctuations in the polarization of the probe can give rise to asymmetry in the resonance signals, which is indistinguishable from real magnetic noise. The stability of the polarization of the probe beam, as measured after the cell, has a flicker-noise characteristic with a magnitude of $700 \mu\text{rad}_{\text{rms}}/\sqrt{\text{Hz}}$ at 1 mHz. By intentionally inducing a large polarization change in the probe beam and

subsequently measuring the magnetometer response, we conclude that the effective magnetic noise associated with probe polarization drift is about $100 \text{ fT}_{\text{rms}}/\sqrt{\text{Hz}}$ at 1 mHz. As with the optical-power fluctuations described previously, the polarization instability of the probe beam is not a dominant limitation for the magnetometer presented here.

After traversing the vapor cell, the probe beam passes through a Wollaston prism, which separates the beam into its orthogonal polarization components. These orthogonal components are measured on separate photodetectors, forming a balanced polarimeter. The optical power on each photodetector can be converted into a polarization-rotation angle via [27,40]

$$\phi = \frac{1}{2} \arcsin \left(\frac{P_1 - P_2}{P_1 + P_2} \right), \quad (1)$$

where P_1 and P_2 are the optical powers on the two photodetectors and ϕ is the polarization-rotation angle. The optical-rotation signal is measured in the frequency domain by demodulating the balanced polarimeter output at $\Omega_m/2\pi$.

IV. OPTIMIZATION

The magnetic-detection limit of the magnetometer is determined by its signal-to-noise ratio; thus, for ultimate performance, one needs to understand the dependence of both signal and noise on key operational settings.

The two-channel demodulated polarimeter signal, containing the AMOR resonance (cf. Fig. 2), has in-phase, $\phi_P(v)$, and quadrature, $\phi_Q(v)$, components. These components are well approximated as the real and imaginary components of a complex Lorentzian lineshape defined by

$$\mathcal{L}(v) = \mathcal{A} \left[\frac{\left(\frac{\Gamma}{2}\right)^2}{(v - v_0)^2 + \left(\frac{\Gamma}{2}\right)^2} + i \frac{\frac{\Gamma}{2}(v - v_0)}{(v - v_0)^2 + \left(\frac{\Gamma}{2}\right)^2} \right], \quad (2)$$

where \mathcal{A} is the amplitude, Γ is the full width at half maximum, and v_0 is the resonant frequency. The maximum slope \mathcal{S} of the quadrature component, ϕ_Q , is given by

$$\mathcal{S} = \lim_{v \rightarrow v_0} \frac{d\phi_Q}{dv} = \frac{2\mathcal{A}}{\Gamma}. \quad (3)$$

Equation (3) is effectively the sensitivity of the magnetometer. This sensitivity is seen to vary as certain operational parameters are changed. Here, we explore how this sensitivity varies with the time-averaged pump and probe power. To understand the origin of this sensitivity variation, we measure the resonant response in each operational setting (cf. Fig. 2) and fit to it an equation of the form of Eq. (2). This allows us to obtain the optical-power dependence of the resonant amplitude \mathcal{A} , resonant width

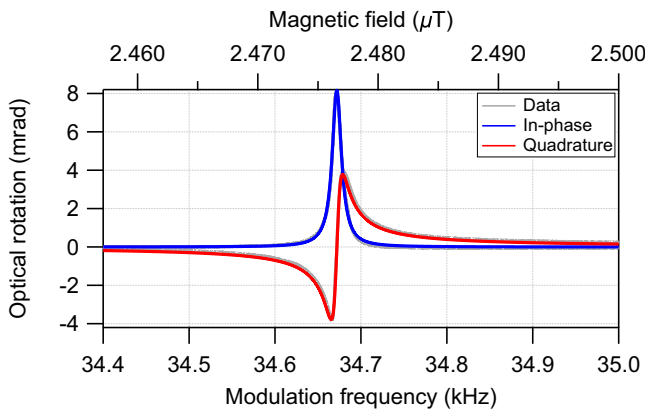


FIG. 2. In-phase and quadrature components of the AMOR resonance measured using time-averaged pump and probe powers of $P_{\text{pump}} = 15 \mu\text{W}$ and $P_{\text{probe}} = 5 \mu\text{W}$ respectively, with a complex Lorentzian fit using Eq. (2). The quadrature component has an amplitude of $\mathcal{A} = 7.57 \text{ mrad}$, a width of $\Gamma = 13.4 \text{ Hz} = 0.96 \text{ nT}$, and a calculated slope of $S = 1.13 \text{ mrad/Hz}$ using Eq. (3). The resonance is centered around a modulation frequency of $\Omega_m/2\pi = 34.672 \text{ kHz}$, corresponding to a magnetic-field strength of $B = 2.4781 \mu\text{T}$.

Γ , and consequently S through Eq. (3). These outcomes are shown across the first three panels of Fig. 3.

Figure 3(a) demonstrates that for low pump power there is a monotonic increase in resonance amplitude, \mathcal{A} , as the pump power is increased. This is reasonable as in this limit the pump power determines the maximum achievable spin polarization. However, for the highest pump powers shown, the atomic response is saturated and we observe a plateau and subsequent decrease of the resonance amplitude [44]. On the other hand, as the probe power increases we observe a monotonic decrease in the resonance amplitude, which is associated with the destruction of ground-state coherence via unwanted optical pumping by the probe [27]. An optimum amplitude is observed at $(P_{\text{pump}}, P_{\text{probe}}) = (30 \mu\text{W}, 3 \mu\text{W})$. By contrast, the resonance width, Γ , presented in

Fig. 3(b), shows a broadening that scales approximately as $\Gamma \propto \sqrt{P_{\text{pump}}^2 + 3P_{\text{probe}}^2}$. Figure 3(c) gives the resulting slope of the resonance in magnetic units, $S\gamma/\pi$, calculated via Eq. (3). The steepest slope (and hence maximum sensitivity) is found at $(P_{\text{pump}}, P_{\text{probe}}) = (7 \mu\text{W}, 3 \mu\text{W})$.

We now turn our attention to the noise of the detection process, which determines the minimum detectable optical rotation per unit bandwidth, $\delta\phi$. Combining this with the slope, S , we obtain the minimum detectable magnetic signal per unit bandwidth, δB :

$$\delta B = \frac{\pi\delta\phi}{S\gamma}, \quad (4)$$

where γ is the gyromagnetic ratio of the ground state. For the $F = 2$ ground state of ^{87}Rb , the gyromagnetic ratio is $\gamma/2\pi = 6.9958 \text{ GHz/T}$ [45].

For all measurements presented here the photodetectors are shot-noise limited. In this case, a beam of light with time-averaged power, P , has a power spectral density as measured at the photodetector of $S(\nu) = 2hvP\eta(\nu)$, where hv is the energy per photon and $\eta(\nu)$ is the quantum efficiency of the photodiode. Therefore, given approximately equal detected powers, P , on the two photodetectors in the polarimeter, the minimum detectable optical rotation per unit bandwidth in the case of shot noise can be calculated from Eq. (1) as $\delta\phi \approx \frac{1}{2}\sqrt{\frac{hv}{\eta(\nu)P}}$. In Fig. 3(d) we combine the signal and noise results to estimate the magnetic-noise floor of the instrument. This indicates an optimum operation point, $(P_{\text{pump}}, P_{\text{probe}}) = (15 \mu\text{W}, 5 \mu\text{W})$, that is not identical to the optimal sensitivity (slope) point seen in Fig. 3(c). The atomic response around the magnetic resonance is shown under these optimal conditions in Fig. 2.

V. PERFORMANCE

The magnetometer performance is examined over a wide range of Fourier frequencies in Fig. 4. For fast fluctuations ($> 0.5 \text{ Hz}$) we characterize this performance by

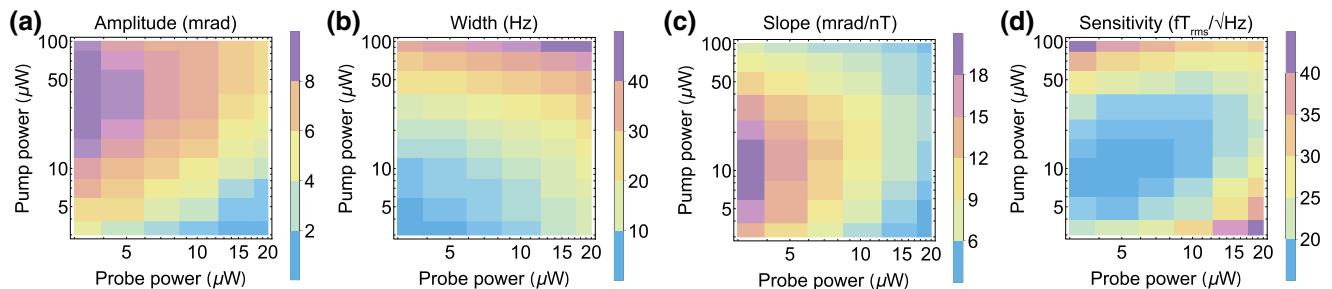


FIG. 3. Optical-power-optimization contour plots for the magnetometer, showing the resonance amplitude \mathcal{A} (a), resonance width Γ (b), resonance slope in magnetic units $S\gamma/\pi$ (c) and the shot-noise-limited sensitivity δB (d). The optimum operating point occurs for time-averaged pump and probe powers of $P_{\text{pump}} = 15 \mu\text{W}$ and $P_{\text{probe}} = 5 \mu\text{W}$, respectively. Using this combination of optical powers results in a shot-noise-limited sensitivity of $15 \text{ fT}_{\text{rms}}/\sqrt{\text{Hz}}$.

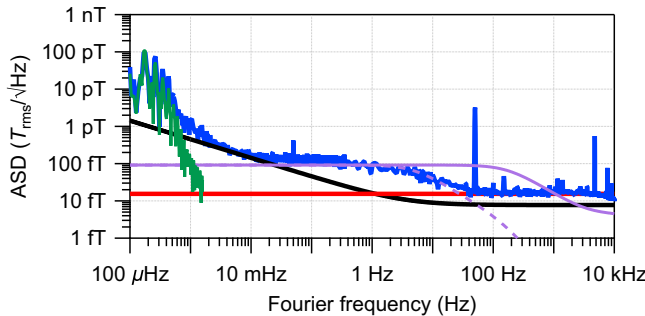


FIG. 4. Amplitude spectral density of the magnetometer noise floor (blue trace) calculated via Welch's method [46], using a 26-h measurement. The noise floor is shot-noise limited (red trace) above 40 Hz, but exhibits excess noise at low Fourier frequencies arising from unwanted fluctuations in the magnetic field at the sensor. In the intermediate frequency range (30 mHz to 40 Hz), Johnson current noise in the solenoid generates magnetic noise (solid purple trace, with a 5-Hz-filtered version shown in the dashed purple trace). Between 1 and 30 mHz, magnetic noise arising from the innermost shield dominates [47] (black trace), while at the lowest frequencies, temperature sensitivity of the solenoid current modulates the magnetic field (green trace). The measured temperature fluctuations of the current source are scaled by an experimentally-determined factor of 100 pT/°C.

directly measuring ϕ_Q with a spectrum analyzer when the pump modulation frequency is tuned to the resonance condition $\Omega_m = 2\Omega_L$. We subsequently convert this signal to an equivalent magnetic fluctuation using Eq. (4). Slow fluctuations (< 0.5 Hz) are measured by actively locking the pump modulation frequency to the magnetic resonance, and then using a frequency counter to measure the variations in pump modulation frequency. Both approaches are shown in Fig. 4 and are in excellent agreement where they overlap.

The key determinant of the read-out system noise is photodetection noise. The bespoke photodetectors used here implement a transimpedance amplifier with a gain of $10^6 \Omega$, and show an effective magnetic noise of about $2 \text{ fT}_{\text{rms}}/\sqrt{\text{Hz}}$ due to the combined dark-current noise of both photodetectors.

The photodetector output signals are then sent to a commercial lock-in amplifier with a measured input noise of $6 \text{ nV}_{\text{rms}}/\sqrt{\text{Hz}}$. Using the experimental parameters reported here, the input noise of the lock-in amplifier gives rise to an effective magnetic noise of $0.4 \text{ fT}_{\text{rms}}/\sqrt{\text{Hz}}$. We note that changes in the phase of the lock-in amplifier can give rise to an asymmetry in the resonance signals, which is indistinguishable from real magnetic fluctuations. The specified phase noise of the lock-in amplifier is about $60 \text{ nrad}_{\text{rms}}/\sqrt{\text{Hz}}$, which corresponds to an effective magnetic noise of about $90 \text{ aT}_{\text{rms}}/\sqrt{\text{Hz}}$.

When measuring high-frequency magnetic-field noise using a spectrum analyzer, the input noise of the spectrum analyzer will give rise to an effective magnetic noise. For

the measurements performed here, this effective noise is consistently below $1 \text{ fT}_{\text{rms}}/\sqrt{\text{Hz}}$ at 1 Hz, dropping as low as $150 \text{ aT}_{\text{rms}}/\sqrt{\text{Hz}}$ at high Fourier frequencies (i.e., above 100 Hz).

When measuring low-frequency magnetic-field noise by actively locking the pump modulation frequency to the magnetic resonance and subsequently observing variations in the modulation frequency, the effective magnetic noise introduced by the frequency counter must also be considered. The noise of the frequency counter is dependent upon both the signal-to-noise ratio of the signal, which it is counting, as well as the gate time. Under the experimental conditions presented here, the measured effective magnetic noise due to the frequency counter is about $2 \text{ fT}_{\text{rms}}/\sqrt{\text{Hz}}$.

The bandwidth of the magnetometer is determined by introducing a small sinusoidal modulation to the applied magnetic field using a high-bandwidth (> 100 kHz) coil wrapped around the center of the solenoid. The magnetometer's response to this modulation is observed by performing a free-induction decay measurement [48], in which the spin-polarized atomic vapor is allowed to relax in the presence of the modulated magnetic field. An example free-induction decay time trace and its corresponding Fourier transform is shown in Fig. 5, for an applied ac

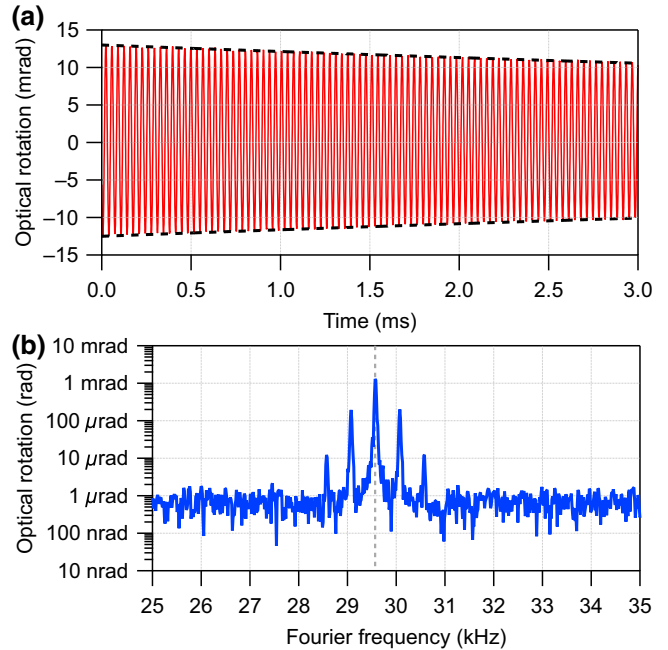


FIG. 5. (a) Free-induction decay measurement performed in the temporal domain, with a carrier frequency of $\Omega_L/\pi = 29.567$ kHz and a small sinusoidal frequency modulation at 500 Hz. Dashed black lines highlight the damped exponential envelope, which has a time constant of 14.5 ms. (b) Fourier transform of the free-induction decay data presented in (a), showing a peak at the carrier frequency of 29.567 kHz (indicated by the dashed vertical line), and both first- and second-order sidebands arising from the sinusoidal modulation at 500 Hz.

magnetic-field strength of 10 nT at a frequency of 500 Hz. The measured transfer function shows that the bandwidth of the magnetometer is greater than 10 kHz.

The photon shot noise, calculated from the measured current from the photodetectors, corresponds to a magnetic noise of $15 \text{ fT}_{\text{rms}}/\sqrt{\text{Hz}}$, and is shown in red in Fig. 4. We see that the measured magnetometer performance is limited by this noise source over a frequency range of 40 Hz to 10 kHz. This corresponds to a dynamic range of the instrument of over $10^8/\sqrt{\text{Hz}}$, which, to the best of our knowledge, is the highest ever reported for an optical magnetometer of any kind.

Evident in the high-frequency region of Fig. 4 is a peak in the noise at 50 Hz and harmonics thereof. The amplitude of this noise component is observed to be largely independent of the number of layers of shielding. Since the high-permeability shields are appropriate for the attenuation of low-frequency magnetic fields via flux shunting, the noise must be originating from within the shields. Given that the measured transfer function of the Butterworth filter is around -100 dB at 50 Hz, the electronics, which drive the solenoid, cannot be the source. We therefore believe that these peaks originate from electromagnetic coupling of ambient magnetic fields through the conductors that connect the solenoid to the driving electronics.

In the intermediate region between 30 mHz and 40 Hz, the performance is limited by Johnson current noise arising in the finite impedance of the solenoid. A SPICE model including the voltage reference, current-setting resistors, and the solenoid (both inductance and resistance) predicts a current noise of $53 \text{ pA}_{\text{rms}}/\sqrt{\text{Hz}}$, corresponding to $92 \text{ fT}_{\text{rms}}/\sqrt{\text{Hz}}$ of magnetic noise (cf. solid purple trace in Fig. 4). The SPICE model also predicts that this Johnson noise should have a low-pass-filter characteristic with a cut-off frequency of 170 Hz. We see excellent agreement between the observed magnetic noise and the model prediction at low frequency; however, the experiment suggests a cut-off frequency close to 5 Hz. The dashed purple trace in Fig. 4 shows the Johnson noise filtered using a 5-Hz low-pass filter. The origin of this difference is unknown; however, we speculate that the distributed nature of the solenoid noise may lead to some additional filtering over that predicted by the lumped-element SPICE model.

For frequencies below 30 mHz, the performance is limited by a combination of two factors: thermal fluctuations of the magnetization of the innermost layer of magnetic shielding [47] (shown by the black trace in Fig. 4), and a temperature sensitivity of the current source that drives the solenoid. We noted a strong correlation between the observed magnetic field and the temperature of both the Butterworth filter and voltage reference. The measured temperature fluctuations are shown in the green trace in Fig. 4, after conversion to magnetic-field units using an experimentally-determined scaling factor of $100 \text{ pT}/^\circ\text{C}$

($\equiv 57 \text{ nA}/^\circ\text{C}$), that was measured independently by deliberately heating the Butterworth filter.

We note that in the region of elevated noise (i.e., below 40 Hz), the observed fluctuations arise not from the sensor itself, but rather from low-level residual fluctuations in the magnetic field generated inside the magnetic shields.

VI. DISCUSSION

A. Measurement limitations

As discussed in Sec. V of the manuscript, the sensitivity across the majority of the Fourier-frequency range presented here is limited by the stability of the measured magnetic field, rather than by the magnetometer itself. All of the present limitations have been identified, and there are a number of avenues remaining to be explored, which may yield increased performance in these areas.

At high Fourier frequencies (i.e., $\gtrsim 40 \text{ Hz}$), the shield noise is only a factor of 2 below the shot-noise limit and hence an improvement in sensitivity of the magnetometer by only a small factor would result in the shield noise limiting the measurement. In this frequency region, the shield noise is associated with Johnson currents arising from the relatively low resistivity of μ -metal. The magnitude of this noise contribution can be reduced through the use of ferrite as the inner layer of shielding, as ferrite shields have been demonstrated to generate up to 25 times less Johnson magnetic noise than that of μ -metal shields of similar dimensions, owing to an electrical resistivity that is as much as 6 orders of magnitude larger than μ -metal [49]. Furthermore, ferrite shields also generate less than half the thermal magnetization noise than their μ -metal counterparts [49], which would reduce the noise that is presently limiting the measurement in the 1 to 30 mHz range.

In the intermediate range between 30 mHz and 40 Hz, the measurement is limited by Johnson current noise arising from the solenoid. SPICE modeling indicates that this noise could be reduced by using a higher-impedance conductor, which would improve the performance over this frequency range.

In the ultralow-frequency range below 1 mHz, the measurement is limited by magnetic noise associated with temperature drift of the coil-driving electronics, as determined by a strong correlation between the observed magnetic field and the temperature of the Butterworth filter and voltage reference. The noise in this region can be effectively suppressed via active temperature stabilization of these components.

B. Magnetometer limitations

The ultimate performance limit of the magnetometer is determined by various noise sources, which are intrinsic to

the device. Many of these sources have been identified and have immediate pathways for improvement.

At high Fourier frequencies (i.e., $\gtrsim 40$ Hz), the magnetometer is limited by photon shot noise. There are two ways in which to improve the performance in this frequency region: by increasing the sensitivity of the magnetometer to changes in magnetic-field strength, and by reducing the effect of shot noise.

The optical rotation experienced by the probe beam may be improved by increasing the optical depth of the vapor via heating the cell. Due to the tradeoff between increasing vapor density, spin-exchange collisions [50], and shot noise, the optimal optical depth is around unity [24]. This optical depth could be achieved with a temperature increase of about 30°C [45], which would yield approximately an order of magnitude increased magnetic sensitivity.

The shot-noise limit could be improved through the use of polarization-squeezed light, which has previously been shown to improve the sensitivity of NMOR magnetometers by 2–3 dB [51,52].

At low frequencies, i.e., below 1 Hz, the two main limitations intrinsic to the magnetometer are the optical-power stability and polarization stability of the probe beam.

The fractional optical-power stability of the probe beam is presently about 100 ppm, which corresponds to an effective magnetic noise of $100 \text{ fT}_{\text{rms}}/\sqrt{\text{Hz}}$ at 1 mHz. Fractional power stabilities on the order of 1 ppm have previously been demonstrated [53], which would reduce the effective magnetic noise due to optical power instability by 2 orders of magnitude if implemented here.

The polarization drift of the probe beam also introduces an effective noise of $100 \text{ fT}_{\text{rms}}/\sqrt{\text{Hz}}$ at 1 mHz, as discussed in Sec. V. This polarization drift is associated with mechanical or thermal alignment drift of the polarization optics with respect to the incident beam. This can, in principle, be improved through the use of mounting materials with low thermal-expansion coefficients [54].

C. Applications

The measurements presented here are performed in a $2.5\text{-}\mu\text{T}$ bias field due to gradient-broadening limitations described in Sec. III. In principle, if the field variations across the cell volume can be minimized, this demonstrated performance can be achieved at geophysical magnetic fields [22].

As it stands, the demonstrated performance of the magnetometer is sufficient for high-sensitivity, high-bandwidth applications such as magnetocardiography [13,55] and magnetoencephalography [55]. These two applications require the measurement of small magnetic fields of around 100 pT and 100 fT, respectively, within a bandwidth of up to 1 kHz [55]. Furthermore, due to the large dynamic

range of this device, these applications may also be possible within Earth's field, thereby removing the need for magnetically shielded rooms. The demonstrated sensitivity on long timescales is also highly suited for low-frequency applications such as the search for plant biomagnetism, which requires resolution of fields less than 60 pT at frequencies around 1 mHz [34].

We envisage that future work will involve measuring small magnetic samples within the shielded environment. For larger samples, the techniques presented here can be readily transferred to an unshielded environment in a similar fashion to a previous demonstration using a SERF magnetometer [56]. However, depending on the magnitude and inhomogeneity of the ambient field, there may be some reduction in sensitivity arising from the nonlinear Zeeman effect [22] and gradient broadening [42], respectively.

VII. CONCLUSION

We develop a magnetometer based on amplitude-modulated nonlinear magneto-optical rotation in ^{87}Rb vapor. Through careful optimization and stabilization of experimental parameters, a $2.5\text{-}\mu\text{T}$ magnetic field is measured with a shot-noise-limited noise floor of $15 \text{ fT}_{\text{rms}}/\sqrt{\text{Hz}}$, corresponding to a fractional sensitivity of $9 \text{ ppb}/\sqrt{\text{Hz}}$. We observe the performance of the magnetometer over 8 orders of magnitude in Fourier frequency, and note that the low-frequency performance is limited by the ability to produce a sufficiently quiet magnetic environment, rather than a limitation of the sensor itself.

ACKNOWLEDGMENTS

The authors acknowledge financial support from the Defence Science and Technology Group, and the South Australian Government through the Premier's Science and Research Fund. The authors wish to express their sincere gratitude to Russell Anderson for editorial support. Additionally, the authors wish to thank Ashby Hilton for his assistance with the SPICE model, as well as Scott Foster and Joanne Harrison for their useful discussions.

-
- [1] V. G. Lucivero, P. Anielski, W. Gawlik, and M. W. Mitchell, Shot-noise-limited magnetometer with sub-picotesla sensitivity at room temperature, *Rev. Sci. Instrum.* **85**, 113108 (2014).
 - [2] I. K. Kominis, T. W. Kornack, J. C. Allred, and M. V. Romalis, A subfemtotesla multichannel atomic magnetometer, *Nature* **422**, 596 (2003).
 - [3] D. Sheng, S. Li, N. Dural, and M. V. Romalis, Sub-femtotesla Scalar Atomic Magnetometry Using Multipass Cells, *Phys. Rev. Lett.* **110**, 160802 (2013).
 - [4] H. B. Dang, A. C. Maloof, and M. V. Romalis, Ultrahigh sensitivity magnetic field and magnetization measurements

- with an atomic magnetometer, *Appl. Phys. Lett.* **97**, 151110 (2010).
- [5] G. Bison, N. Castagna, A. Hofer, P. Knowles, J.-L. Schenker, M. Kasprzak, H. Saudan, and A. Weis, A room temperature 19-channel magnetic field mapping device for cardiac signals, *Appl. Phys. Lett.* **95**, 173701 (2009).
- [6] G. Bison, R. Wynands, and A. Weis, A laser-pumped magnetometer for the mapping of human cardiomagnetic fields, *Appl. Phys. B* **76**, 325 (2003).
- [7] S. Knappe, T. H. Sander, O. Kosch, F. Wiekhorst, J. Kitching, and L. Trahms, Cross-validation of microfabricated atomic magnetometers with superconducting quantum interference devices for biomagnetic applications, *Appl. Phys. Lett.* **97**, 133703 (2010).
- [8] C. Johnson, P. D. D. Schwindt, and M. Weisend, Magnetoencephalography with a two-color pump-probe, fiber-coupled atomic magnetometer, *Appl. Phys. Lett.* **97**, 243703 (2010).
- [9] S. Xu, V. V. Yashchuk, M. H. Donaldson, S. M. Rochester, D. Budker, and A. Pines, Magnetic resonance imaging with an optical atomic magnetometer, *Proc. Natl. Acad. Sci. USA* **103**, 12668 (2006).
- [10] E. Boto, N. Holmes, J. Leggett, G. Roberts, V. Shah, S. S. Meyer, L. D. Muñoz, K. J. Mullinger, T. M. Tierney, S. Bestmann, G. R. Barnes, R. Bowtell, and M. J. Brookes, Moving magnetoencephalography towards real-world applications with a wearable system, *Nature* **555**, 657 (2018).
- [11] K. Jensen, M. A. Skarsfeldt, H. Strkind, J. Arnbak, M. V. Balabas, S.-P. Olesen, B. H. Bentzen, and E. S. Polzik, Magnetocardiography on an isolated animal heart with a room-temperature optically pumped magnetometer, *Sci. Rep.* **8**, 16218 (2018).
- [12] J. Belfi, G. Bevilacqua, V. Biancalana, S. Cartaleva, Y. Dancheva, and L. Moi, Cesium coherent population trapping magnetometer for cardiosignal detection in an unshielded environment, *J. Opt. Soc. Am. B* **24**, 2357 (2007).
- [13] G. Bison, R. Wynands, and A. Weis, Dynamical mapping of the human cardiomagnetic field with a room-temperature, laser-optical sensor, *Opt. Express* **11**, 904 (2003).
- [14] H. Xia, A. Ben-Amar Baranga, D. Hoffman, and M. V. Romalis, Magnetoencephalography with an atomic magnetometer, *Appl. Phys. Lett.* **89**, 211104 (2006).
- [15] O. Alem, T. H. Sander, R. Mhaskar, J. LeBlanc, H. Eswaran, U. Steinhoff, Y. Okada, J. Kitching, L. Trahms, and S. Knappe, Fetal magnetocardiography measurements with an array of microfabricated optically pumped magnetometers, *Phys. Med. Biol.* **60**, 4797 (2015).
- [16] M. Smiciklas, J. M. Brown, L. W. Cheuk, S. J. Smullin, and M. V. Romalis, New Test of Local Lorentz Invariance Using a ^{21}Ne -Rb-K Comagnetometer, *Phys. Rev. Lett.* **107**, 171604 (2011).
- [17] C. J. Berglund, L. R. Hunter, D. Krause, Jr., E. O. Prigge, M. S. Ronfeldt, and S. K. Lamoreaux, New Limits on Local Lorentz Invariance from Hg and Cs Magnetometers, *Phys. Rev. Lett.* **75**, 1879 (1995).
- [18] S. Pustelny, D. F. Jackson Kimball, C. Pankow, M. P. Ledbetter, P. Włodarczyk, P. Wcislo, M. Pospelov, J. R. Smith, J. Read, W. Gawlik, and D. Budker, The global network of optical magnetometers for exotic physics (GNOME): A novel scheme to search for physics beyond the standard model, *Ann. Phys.* **525**, 659 (2013).
- [19] D. F. Jackson Kimball, I. Lacey, J. Valdez, J. Swiatlowski, C. Rios, R. Peregrina-Ramirez, C. Moncrieffe, J. Kremer, J. Dudley, and C. Sanchez, A dual-isotope rubidium comagnetometer to search for anomalous long-range spin-mass (spin-gravity) couplings of the proton, *Ann. Phys.* **525**, 514 (2013).
- [20] D. Budker, D. F. Jackson Kimball, S. M. Rochester, V. V. Yashchuk, and M. Zolotorev, Sensitive magnetometry based on nonlinear magneto-optical rotation, *Phys. Rev. A* **62**, 043403 (2000).
- [21] J. C. Allred, R. N. Lyman, T. W. Kornack, and M. V. Romalis, High-Sensitivity Atomic Magnetometer Unaffected by Spin-Exchange Relaxation, *Phys. Rev. Lett.* **89**, 130801 (2002).
- [22] V. Acosta, M. P. Ledbetter, S. M. Rochester, D. Budker, D. F. Jackson Kimball, D. C. Hovde, W. Gawlik, S. Pustelny, J. Zachorowski, and V. V. Yashchuk, Nonlinear magneto-optical rotation with frequency-modulated light in the geophysical field range, *Phys. Rev. A* **73**, 053404 (2006).
- [23] D. Budker, D. F. Jackson Kimball, V. V. Yashchuk, and M. Zolotorev, Nonlinear magneto-optical rotation with frequency-modulated light, *Phys. Rev. A* **65**, 055403 (2002).
- [24] S. Pustelny, A. Wojciechowski, M. Gring, M. Kotyra, J. Zachorowski, and W. Gawlik, Magnetometry based on nonlinear magneto-optical rotation with amplitude-modulated light, *J. Appl. Phys.* **103**, 063108 (2008).
- [25] E. Breschi, Z. D. Grujić, P. Knowles, and A. Weis, A high-sensitivity push-pull magnetometer, *Appl. Phys. Lett.* **104**, 023501 (2014).
- [26] A. Wojciechowski, E. Corsini, J. Zachorowski, and W. Gawlik, Nonlinear Faraday rotation and detection of superposition states in cold atoms, *Phys. Rev. A* **81**, 053420 (2010).
- [27] W. Gawlik and S. Pustelny, *High Sensitivity Magnetometers* (Springer, Switzerland, 2017), p. 425.
- [28] D. Budker, W. Gawlik, D. F. Jackson Kimball, S. M. Rochester, V. V. Yashchuk, and A. Weis, Resonant nonlinear magneto-optical effects in atoms, *Rev. Mod. Phys.* **74**, 1153 (2002).
- [29] D. Budker and M. Romalis, Optical magnetometry, *Nat. Phys.* **3**, 227 (2007).
- [30] A. Sheinker, L. Frumkis, B. Ginzburg, N. Salomonski, and B.-Z. Kaplan, Magnetic anomaly detection using a three-axis magnetometer, *IEEE Trans. Magn.* **45**, 160 (2009).
- [31] M. Hayakawa, K. Hattori, and K. Ohta, Monitoring of ULF (ultra-low-frequency) geomagnetic variations associated with earthquakes, *Sensors* **7**, 1108 (2007).
- [32] M. Hayakawa, R. Kawate, O. A. Molchanov, and K. Yumoto, Results of ultra-low-frequency magnetic field measurements during the Guam Earthquake of 8 August 1993, *Geophys. Res. Lett.* **23**, 241 (1996).
- [33] A. C. Fraser-Smith, A. Bernardi, P. R. McGill, M. E. Ladd, R. A. Helliwell, and O. G. Villard, Jr., Low-frequency magnetic field measurements near the epicenter of the M_s

- 7.1 Loma Prieta Earthquake, *Geophys. Res. Lett.* **17**, 1465 (1990).
- [34] E. Corsini, V. Acosta, N. Baddour, J. Higbie, B. Lester, P. Licht, B. Patton, M. Prouty, and D. Budker, Search for plant biomagnetism with a sensitive atomic magnetometer, *J. Appl. Phys.* **109**, 074701 (2011).
- [35] I. Mateos, B. Patton, E. Zhivun, D. Budker, D. Wurm, and J. Ramos-Castro, Noise characterization of an atomic magnetometer at sub-millihertz frequencies, *Sens. Actuators, A* **224**, 147 (2015).
- [36] M. Schmelz, R. Stolz, V. Zakosarenko, T. Schönau, S. Anders, L. Fritzsch, M. Mück, and H.-G. Meyer, Field-stable SQUID magnetometer with sub-fT Hz^{-1/2} resolution based on sub-micrometer cross-type Josephson tunnel junctions, *Supercond. Sci. Technol.* **24**, 065009 (2011).
- [37] D. Drung, Low-frequency noise in low- T_c multiloop magnetometers with additional positive feedback, *Appl. Phys. Lett.* **67**, 1474 (1995).
- [38] E. B. Alexandrov, M. Auzinsh, D. Budker, D. F. Jackson Kimball, S. M. Rochester, and V. V. Yashchuk, Dynamic effects in nonlinear magneto-optics of atoms and molecules, *J. Opt. Soc. Am. B* **22**, 7 (2005).
- [39] N. Wilson, N. B. Hébert, C. Perrella, P. Light, J. Genest, S. Pustelny, and A. Luiten, Simultaneous Observation of Nonlinear Magneto-Optical Rotation in the Temporal and Spectral Domains with an Electro-Optic Frequency Comb, *Phys. Rev. Appl.* **10**, 034012 (2018).
- [40] W. Gawlik and S. Pustelny, *New Trends in Quantum Coherence and Nonlinear Optics* (Nova Publishers, New York, 2009), p. 47.
- [41] T. J. Sumner, J. M. Pendlebury, and K. F. Smith, Convectional magnetic shielding, *J. Phys. D* **20**, 1095 (1987).
- [42] S. Pustelny, D. F. Jackson Kimball, S. M. Rochester, V. V. Yashchuk, and D. Budker, Influence of magnetic-field inhomogeneity on nonlinear magneto-optical resonances, *Phys. Rev. A* **74**, 063406 (2006).
- [43] D. W. Allan, Statistics of atomic frequency standards, *Proc. IEEE* **54**, 221 (1966).
- [44] M. Auzinsh, D. Budker, and S. M. Rochester, *Optically Polarized Atoms* (Oxford University Press, New York, 2010).
- [45] D. A. Steck, Rubidium 87 D Line Data, <http://steck.us/alkalidata>, note (revision 2.1.5, 13 September 2018).
- [46] P. Welch, The use of fast Fourier transform for the estimation of power spectra: A method based on time averaging over short, modified periodograms, *IEEE Trans. Audio Electroacoust.* **15**, 70 (1967).
- [47] S.-K. Lee and M. V. Romalis, Calculation of magnetic field noise from high-permeability magnetic shields and conducting objects with simple geometry, *J. Appl. Phys.* **103**, 084904 (2008).
- [48] D. Hunter, S. Piccolomo, J. D. Pritchard, N. L. Brockie, T. E. Dyer, and E. Riis, Free-Induction-Decay Magnetometer Based on a Microfabricated Cs Vapor Cell, *Phys. Rev. Appl.* **10**, 014002 (2018).
- [49] T. W. Kornack, S. J. Smullin, S.-K. Lee, and M. V. Romalis, A low-noise ferrite magnetic shield, *Appl. Phys. Lett.* **90**, 223501 (2007).
- [50] M. T. Graf, D. F. Jackson Kimball, S. M. Rochester, K. Kerner, C. Wong, D. Budker, E. B. Alexandrov, M. V. Balabas, and V. V. Yashchuk, Relaxation of atomic polarization in paraffin-coated cesium vapor cells, *Phys. Rev. A* **72**, 023401 (2005).
- [51] F. Wolfgramm, A. Cerè, F. A. Beduini, A. Predojević, M. Koschorreck, and M. W. Mitchell, Squeezed-Light Optical Magnetometry, *Phys. Rev. Lett.* **105**, 053601 (2010).
- [52] T. Horrom, R. Singh, J. P. Dowling, and E. E. Mikhailov, Quantum-enhanced magnetometer with low-frequency squeezing, *Phys. Rev. A* **86**, 023803 (2012).
- [53] F. Tricot, D. H. Phung, M. Lours, S. Guérandel, and E. de Clercq, Power stabilization of a diode laser with an acousto-optic modulator, *Rev. Sci. Instrum.* **89**, 113112 (2018).
- [54] H. Duncker, O. Hellwig, A. Wenzlawski, A. Grote, A. J. Rafipoor, M. Rafipoor, K. Sengstock, and P. Windpassinger, Ultrastable, Zerodur-based optical benches for quantum gas experiments, *Appl. Opt.* **53**, 4468 (2014).
- [55] *Magnetism in Medicine*, edited by W. Andrä and H. Nowak (Akademie Verlag, Weinheim, Germany, 2007), 2nd ed.
- [56] S. J. Seltzer and M. V. Romalis, Unshielded three-axis vector operation of a spin-exchange-relaxation-free atomic magnetometer, *Appl. Phys. Lett.* **85**, 4804 (2004).